JOURNAL OF SPACECRAFT AND ROCKETS
Vol. 43, No. 6, November–December 2006

Simulation of Aerodynamic Influences on Rocket-Mounted Oxygen Sensors

Jeffrey B. Allen,* Mark Perl,† and Thomas Hauser‡
Utah State University, Logan, Utah, 84322-4130

DOI: 10.2514/1.19060

Over the past several decades, atomic oxygen measurements taken from sounding rocket sensor payloads in the altitude range of 80–140 kilometers have shown marked variability. Many sounding rocket payloads contain atomic oxygen sensors that are located in close proximity to the payload surface, and are thus significantly influenced by flow field disturbances. Although several additional factors including Doppler shift and sensor contamination may also play a significant role in the accurate measurement of atomic oxygen concentrations, this work focuses solely on the effects due to the flow field. The present study utilizes the three-dimensional, steady-state, direct simulation Monte Carlo technique. In addition, the lower altitudes corresponding to near-continuum flow are solved via the Navier–Stokes equations with slip wall boundary conditions. The flow is simulated at 13 different altitudes, each with three separate rocket orientations, along both the rocket's upleg and downleg trajectory for a total of 75 simulations. The numerical simulations show conclusively that the relative magnitudes of undisturbed versus disturbed atomic oxygen concentrations are highly dependent upon rocket orientation, and provide a quantitative means by which existing atomic oxygen concentration data sets may be corrected for aerodynamic influences.

Nomenclature

c	=	speed of sound
F, G, H	=	Cartesian flux vector of the Navier–Stokes equations
e	=	energy per unit mass
f_{ram}	=	density correction factor
g	=	tangential
Kn	=	Knudsen number
k	=	coefficient of thermal conductivity
L	=	rocket diameter
M	=	Mach number
N	=	number of simulated molecules
N_2	=	nitrogen
n	=	number density
O	=	atomic oxygen
O_3	=	ozone
p	=	pressure
$\boldsymbol{q}$	=	heat flux vector
Re	=	Reynolds number
T	=	temperature
u, v, w	=	Cartesian velocity components
x, y, z	=	Cartesian coordinate components
α	=	angle of attack
λ	=	molecular mean free path
μ	=	dynamic viscosity
ρ	=	density
σ_v	=	velocity accommodation coefficient
τ	=	stress tensor

Subscripts

∞	=	freestream conditions
meas	=	measured value
r	=	relative
w	=	wall

Presented as Paper 5287 at the 35th AIAA Fluid Dynamics Conference and Exhibit, Toronto, Ontario, Canada, , 6–9 June 2005; received 18 October 2005; revision received 25 December 2005; accepted for publication 12 January 2006.

*Graduate Research Assistant, Department of Mechanical & Aerospace Engineering, Student Member AIAA.

†Undergraduate Student, Department of Mechanical & Aerospace Engineering.

‡Assistant Professor, Department of Mechanical & Aerospace Engineering, Member AIAA.

I. Introduction

THE altitude range between 80 and 140 km is known as the Earth's mesosphere and lower thermosphere. Scientific interests in this regime surround a wide variety of complex atmospheric phenomena. Of particular interest is the study of atomic oxygen concentrations. The correct assessment of atomic oxygen concentrations in the lower thermosphere is important for a large number of reasons, principal among these include the creation of ozone (O_3), the expansion and contraction of the atmosphere, and global climate change [1].

Among the various means of measuring atomic oxygen concentration in the lower thermosphere, in situ measurements using sensor platforms aboard sounding rockets have proven very useful in providing vertical resolution over the entire collection period. Unfortunately, however, sounding rocket data taken over the past few decades have shown significant variability in atomic oxygen concentrations, amounting to uncertainties of more than 2 orders of magnitude at certain altitudes [2].

Several challenges inhibit accurate freestream number density measurements by the atomic oxygen sensors which are often located within close proximity to the payload surface. The primary challenges include Doppler shifts due to rocket motion, sensor contamination due to venting and outer surface desorption, and flow field disturbances [3]. Therefore, it is of major importance to understand the aerodynamic effects on the flow field around the payload. Despite this importance, experiments or flow simulations which fully take into account the flow field influences are rather limited.

In this paper, we describe a procedure to quantify the aerodynamic influence of the supersonic motion on the measurements through detailed three-dimensional numerical simulations. First, we give a description of the experiment and the aerodynamic problem. We introduce a so-called ram-factor [1], as the ratio between the density actually measured by the gauge and the undisturbed density of the flow. Three-dimensional results using the direct simulation Monte Carlo method (DSMC) are used to determine the altitude

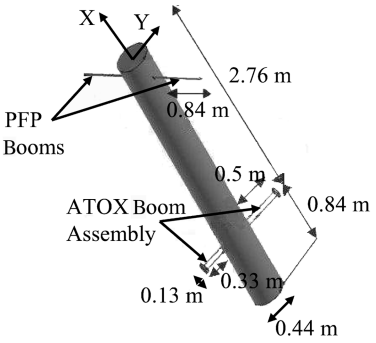

a) CODA payload geometry with origin and upper and lower boom assemblies

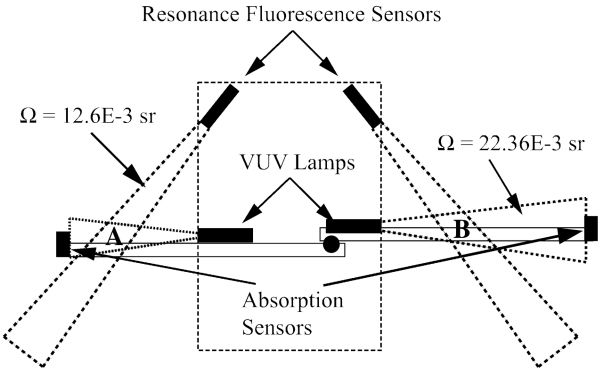

b) The USU ATOX sensor, showing absorption/emission volumes of the resonance fluorescence sensors and lamps, respectively

Fig. 1 CODA payload geometry and USU ATOX sensor.

profile of ram-factors for different sensor orientations. Finally, we apply the ram-factor correction to determine mean density profiles of atomic oxygen for the CODA (coupling of dynamics and aurora) I and II missions.

II. CODA Experiment

Data used for this research were collected during two separate flights of the CODA program. The missions were sponsored by NASA under contract number NAG5-5187. The CODA missions were designed specifically to investigate the effects of an active aurora on the turbulence and vertical mixing that plays such a critical role in atomic oxygen concentrations [4]. Both of the CODA flights originated from the University of Alaska's Poker Flat Research Range (65° north latitude, 147° west longitude), followed similar trajectories, and landed roughly 250 km to the north/northwest. CODA I (21.121) was launched on 22 Jan. 1999 at 15:20 UMT (06:20 local) and reached an apogee of 136.47 km, while CODA II (21.128) was launched on 21 Feb. 2002 at 09:55 UMT (00:55 local) and reached an apogee of 139.74 km [4].

A. ATOX Sensor

The present work is based upon sensor measurements taken with Utah State University's (USU) version of the resonant fluorescence/absorption sensor system, referred to as ATOX [5], and will be specifically applied to the CODA payload geometry shown in Fig. 1 (applicable to both CODA I & II). Figure 1a shows the rocket geometry after ejection of the nose cone. The two top booms contain the plasma frequency probe (PFP) and the asymmetric bottom booms contain the ATOX sensor assembly. Figure 1a shows the surface of the modeled geometry. Because this paper discusses the correction of data for the ATOX sensor, Fig. 1b shows the ATOX sensing geometry in more detail. The resonant fluorescence/absorption technique, which has been used both in the laboratory and the atmosphere, relies on the output of the 130-nm wavelength triplet from atomic line sources (lamps) to initiate the measurement [5].

The lamps electronically excite internal oxygen atoms that emit the vacuum ultraviolet (VUV) wavelength triplet as sources within the rocket payload [6–8]. As depicted in Fig. 1b, the emitted radiation is broadcast over a small atmospheric volume surrounding the payload. Boom-mounted photometers measure the radiated energy that passes through the volume unabsorbed, whereas payload-mounted photometers monitor the small portion of energy that is absorbed and reradiated by oxygen atoms within the measurement volume [9]. Volumes A and B are the sensor volumes and our simulations use averages over those small volumes to determine the numerical atomic oxygen concentration. To reduce background radiation from airglow or aurora, the lamp output is modulated at 125 Hz with a 50% duty cycle. The background is subtracted from the signal as part of the data reduction process. The absorption and resonant fluorescence measurements are complementary. The resonant fluorescence photometers provide a highly sensitive concentration measurement of the region, whereas the absorption photometers provide a direct calibration throughout the flight [6,7]. Utilizing outputs from both resonant fluorescence and absorption photometry make it possible to ascertain the concentration of atomic oxygen within the lower thermosphere region.

The orientation of the sensors in the rest of this paper is referenced with respect to the long ATOX boom. The following three orientations are defined as follows:

1) ram, the long ATOX boom is oriented in the direction of the horizontal velocity of the sounding rocket;

2) crosstrack, the long ATOX boom is rotated 90 deg from the ram direction;

3) wake, the long ATOX boom is rotated 180 deg from the ram direction.

B. Oxygen Data

Data used for this research were collected during two separate flights of the CODA program and may be seen in Fig. 2. Data acquisition began at an altitude of approximately 69.1 km and ended at approximately 60.2 km. The payload maintained a constant frequency about its longitudinal axis of 1 revolution/s, and also maintained a constant attitude angle of 60.9 deg. As indicated from the raw data sets in Fig. 2, the effect of orientation of the ATOX sensor on the atomic oxygen concentration is highly significant. In Fig. 2, the number density of the atomic oxygen shown is normalized by the maximum value measured.

The normalized number density of CODA I varies between the wake and ram by as much as 96% in the upleg and downleg. The variation in concentration of CODA II is even more pronounced in the wake as opposed to the ram with 78% upleg and 139% downleg. The variation of the disturbed atomic oxygen concentration in the upleg as opposed to the downleg trajectory is also apparent.

III. Numerical Method

A. Geometry and Grids

As indicated in Fig. 1, the ATOX booms extend approximately 0.5 m and 0.33 m on opposite sides of the fuselage. The original intent for this asymmetrical ATOX boom design was to counter the effects of the flow field by simultaneously measuring the atomic oxygen concentrations in both the ram and wake directions and extrapolating the freestream concentration. Unfortunately, the outcome merely resulted in two independent measurements without a means for accurate extrapolation (at least one that could be conclusively proven).

The resonance fluorescence sensors are located approximately 0.13 m forward of the booms and are inclined at 45 deg to the fuselage wall. As indicated in Fig. 1b, the resonance fluorescence sensors create a solid angle of 12.6E-3 sr. The intersection of this volume with that of the 22.36E-3 sr volume created by the VUV lamps are marked as positions "A" and "B" in Fig. 1b, and constitute the atomic oxygen concentration measurement volume.

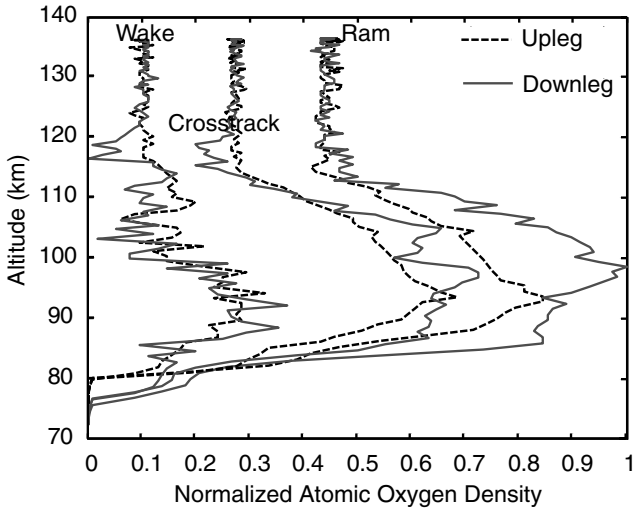

a) CODA I

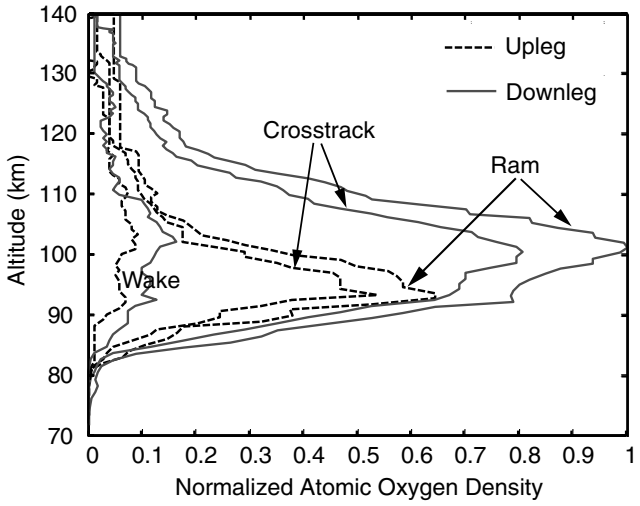

b) CODA II

Fig. 2 Values from ATOX sensor for CODA I and II missions.

As illustrated in Fig. 1, the payload consists of a uniform cylinder with both upper and lower boom assemblies. The nose cone was ejected before data acquisition and was thus not modeled.

The DSMC payload surface mesh is shown in Fig. 3. The mesh was completed using the commercial software package GRIDGEN [10], using 4248 triangular surface elements. Both oxygen sensor boom assemblies were gridded as shown in Fig. 3b. These surface elements served as sampling locations for the macroscopic properties along the payload surface and thus were initially distributed with side lengths no greater than the mean free path associated with 80 km. Upwards of 80 km the number of surface elements remained unchanged for purposes of convenience.

B. Atmospheric Model and Inflow Condition

The Knudsen number based on rocket diameter ($Kn_{\infty,L}$) for the altitudes of interest in this work, as well as all initial conditions applicable to the DSMC method and Navier–Stokes equations with slip wall boundary conditions method (NS-slip) are shown in Tables 1 and 2. The freestream number densities n_∞ and freestream temperatures T_∞ were obtained via the mass-spectrometer incoherent-scatter (MSISE-00) model [11] corresponding to the initial launch time and location described in Sec. II. The species fractions corresponding to O, O_2, and N_2, the angles of attack, and the mean free path λ_∞ corresponding to the variable hard sphere method are also given in Table 1.

The simulations to correct for mission data were conducted over 5 km intervals along the upleg trajectory, beginning with 80 km. The angle of attack for the upleg and downleg, as well as the surface temperature T_S, are given in Table 2. The surface temperature of the rocket's main body was obtained from onboard sensors. We also show the Mach and Knudsen $Kn_\infty L$ in Table 2 as a function of altitude.

The data in Table 2 suggest that the lower altitudes (80–90 km) of this study exhibit flow conditions with Knudsen numbers below the lower limit of the DSMC efficiency range. These altitudes fall within the "slip flow" regime ($0.001 < Kn < 0.1$), and have in past studies been successfully modeled using the Navier–Stokes equations with slip wall boundary conditions. First-order slip conditions for both velocity and temperature conditions at the wall were first developed by Maxwell [12]. Previous studies [13] have shown that first-order slip conditions (in lieu of higher order) are acceptable within this regime. Therefore, the present study uses both the DSMC and the NS-slip method at these lower altitudes to compare the results of both approaches in the slip flow regime.

C. DSMC Method

The external flow field simulations were conducted using the DSMC technique [14]. The method has become de facto the main tool for the study of complex multidimensional flows of rarefied supersonic/hypersonic aerothermodynamics [15]. The DSMC method has been successfully applied to study the external flows of many spacecraft including the Space Shuttle Orbiter [16], the Magellan Spacecraft [17], and the Mars Pathfinder [18].

The DSMC method is well suited for low density flows, and maintains good efficiency for three-dimensional simulations with freestream Knudsen numbers of the order of 0.1 or larger [19]. At

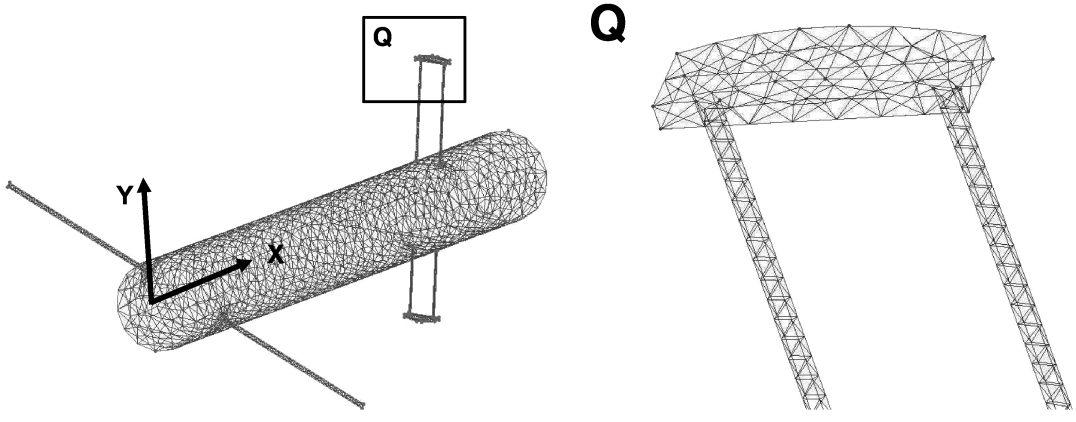

a) Surface mesh of the rocket **b) Surface mesh detail of the oxygen sensor assembly**

Fig. 3 DSMC payload mesh showing detail of lower ATOX boom assembly.

Table 1 DSMC and NS-slip simulations from the atmospheric model as function of altitude

H, km	n_∞, m^{-3}	O	O_2	N_2	λ_∞, m	T_∞, K
80	2.71E20	1.35E − 5	0.210	0.790	0.004	209.3
85	1.24E20	3.56E − 4	0.209	0.791	0.009	202.8
90	5.61E19	0.003	0.205	0.792	0.021	194.5
95	2.46E19	0.015	0.198	0.787	0.047	187.1
100	1.02E19	0.039	0.184	0.777	0.114	188.6
105	4.09E18	0.074	0.165	0.762	0.291	208.5
110	1.71E18	0.116	0.141	0.743	0.731	249.3
115	7.87E17	0.160	0.119	0.721	1.688	311.3
120	4.06E17	0.201	0.100	0.699	3.486	393.4
125	2.40E17	0.237	0.067	0.677	6.188	473.7
130	1.58E17	0.267	0.077	0.656	9.767	543.4
135	1.11E17	0.296	0.070	0.635	14.32	605.5
139.7	8.18E16	0.322	0.064	0.614	19.90	660.5

Table 2 Trajectory of the CODA II mission as a function of altitude

H, km	T_S, K (upleg)	T_S, K (downleg)	M	$\|Kn_{\infty L}$	α, deg (upleg)	α, deg (downleg)
80	346.15	379.15	4.66	0.010	9.01	112.9
85	353.15	379.15	4.61	0.022	10.28	111.5
90	356.15	379.15	4.57	0.047	11.69	110.1
95	363.15	379.15	4.51	0.107	13.26	108.7
100	365.15	379.15	4.35	0.258	15.04	106.7
105	368.15	380.15	3.99	0.662	17.07	104.7
110	371.15	381.15	3.53	1.662	19.16	102.65
115	373.15	382.15	3.02	3.836	22.24	99.55
120	374.15	383.15	2.57	7.923	25.65	96.22
125	376.15	383.15	2.23	14.06	30.01	92.37
130	378.15	383.15	1.97	22.20	35.86	85.66
135	380.15	383.15	1.76	32.53	45.30	77.39
139.7	381.15	381.15	1.62	45.23	60.89	60.89

smaller Knudsen numbers, the method remains valid, although it becomes increasingly computationally expensive. The gas is modeled using a representative number of simulated molecules such that each simulated molecule represents a certain number of "real" molecules. The position and velocity of each of these simulated molecules as a result of intermolecular collisions and boundary interactions is stored through successive time steps. A principle approximation of the method is to assign a time step smaller than the mean time between collisions. This enables the molecular movement to be uncoupled from the intermolecular collisions.

The three-dimensional, steady-state DSMC code, DS3G (version 1.1) [20] is used in this study. The gas was composed of atomic oxygen, gaseous oxygen, and gaseous nitrogen; with species fractions as appropriate to altitude (see Table 1). The molecular collisions of the species were modeled as variable hard spheres such that the sphere radius was proportional to relative speed c_r. Surface interactions were assumed fully diffusive, with complete accommodation of the gas to the prescribed surface temperature.

The selection of the proper number of simulated molecules, which is analogous to obtaining grid independent solutions in grid based methods, was verified using two sets of data along the upleg trajectory and separated along 10 km intervals. The first consisted of approximately 2.0E6 simulated molecules, whereas the second consisted of approximately 6.0E6 molecules. The comparison between these two simulations was conducted with respect to the average atomic oxygen concentration in volume "B". The average percent difference between the two simulations was approximately 3.3% with the largest percent difference (16%) occurring at the 120 km wake location. For this reason, the 120 km wake case was again simulated with 8.0E6 simulated molecules and the result was found to contain less than 3% error. Thus, 6.0E6 simulated molecules were used throughout the upleg and downleg trajectories along 5 km intervals. The simulations were conducted using an average of 12 molecules per cell. Following the recommendations of Bird [14], acceptable results are obtained from an average of at least 10 molecules per cell. The computational domain volume pertaining to the altitudes less than 110 km was approximately 80 m^3, whereas the remaining altitudes were simulated with a volume of approximately 96 m^3. The volume increase at higher altitudes was due to increased rarefaction, and the accompanying diffusivity of the disturbed flow field. The sub cell technique was utilized, wherein the average number of sub cells/cell was four. This technique was used to ensure that intermolecular collisions only occur between molecules within λ. All boundaries were specified as uniform stream boundaries.

Molecules were moved through a time step of one-fifth the local mean collision time which is the near optimum value[14]. Steady-state conditions were monitored at each altitude, and were obtained after sufficiently long times such that the temporal variation of the density profile ($x = 2.0$, $y > 0.2$, $z = 0$) was less than 1%. The average running time was 12 h using a dual processor AMD Opteron 1.40 GHz machine.

D. Navier–Stokes Method

The steady, three-dimensional conservation equations without body forces, expressed in conservative form are presented in Eq. (2).

$$F_x + G_y + H_z = 0 \tag{1}$$

Where F, G, and H represent the flux column vectors in x, y, and z direction, respectively. For example, the flux in x direction is

$$F_x = \begin{Bmatrix} \rho u \\ \rho u^2 + p - \tau_{xx} \\ \rho v u - \tau_{xy} \\ \rho w u - \tau_{xz} \\ \rho\left(e + \frac{V^2}{2}\right)u + pu + \boldsymbol{q}_x - u\tau_{xx} - v\tau_{xy} - w\tau_{xz} \end{Bmatrix} \tag{2}$$

These equations are general and can be applied to both continuum and noncontinuum flows. It is only when approximations are substituted for the heat flux vector and the shear stress tensor that

these equations lose their generality [21]. The Navier–Stokes approximations can be obtained via a first-order expansion of the Boltzmann equation in powers of the Knudsen number. The approximations for the shear stress and heat flux vector become

$$\tau_{ij} = \mu\left[\left(\frac{\partial u_i}{\partial x_j} + \frac{\partial u_j}{\partial x_i}\right) - \frac{2}{3}\delta_{ij}\frac{\partial u_k}{\partial xk}\right] \tag{3}$$

$$\boldsymbol{q} = -k\nabla T \tag{4}$$

To complete the equation set, an ideal gas approximation was used. This approximation was based on the relatively low temperatures and densities of the flow as given in Table 1.

Although the first-order slip wall boundary conditions developed by Maxwell [12] include thermal changes at the wall, for the present work, the wall was assumed isothermal. The justification for this assumption was based on the near constant recorded surface temperatures at the lower altitudes shown in Table 1. The first-order, isothermal slip wall boundary conditions can therefore be represented as

$$u_g - u_w = \frac{2-\sigma_v}{\sigma_v}\lambda\left(\frac{\partial u}{\partial \eta}\right)_{\text{wall}} \tag{5}$$

Where u_g and u_w represent the tangential velocities of the gas and that of the moving wall, respectively. The quantity σ_v is the velocity accommodation coefficient which is approximately one. The term $(\frac{\partial u}{\partial \eta})_{\text{wall}}$ is proportional to the wall shear stress.

The Reynolds number based on rocket diameter ($Re_{\infty,L}$) can be calculated from the Knudsen and Mach numbers as follows:

$$Re_{\infty,L} = \frac{16}{5}\left(\frac{\gamma}{2\pi}\right)^{\frac{1}{2}}\frac{M}{Kn} \tag{6}$$

The $Re_{\infty,L}$ corresponding to 80 and 90 km was calculated and resulted in 506.4 and 103.2, respectively. The simulations were thus solved under laminar flow conditions.

The Navier–Stokes solutions were obtained using a three-dimensional computational domain, initially consisting of approximately 160,000 tetrahedral cells. Because of the complex geometry involved, and the large difference in length scales between the main cylinder body and the ATOX booms, a very fine grid was generated near the payload then stretched to the outer boundary of the computational domain. The average mesh skewness was approximately 0.4 and no cells were found with a skewness greater than 0.8. The boundary conditions consisted of far-field, and outlet pressure conditions as are typical for compressible, ideal gas flows.

The simulations were carried out using FLUENT version 6.1 (http://www.fluent.com). The coupled, implicit solver was used, with second-order upwind differencing. The flow was initialized using the parameters from Table 1. An adaptive grid strategy was employed wherein refinements/coarsening were made relative to flow density gradients. This refined the grid in the areas of the shock and other regions of strong density gradients. The grid adaptations were altitude/orientation dependent, but resulted in an average increase in the number of cells to approximately 250,000. No sensitivity studies were performed because the converged DSMC simulations showed good agreement with the Navier–Stokes simulations.

IV. Aerodynamic Effects Along the Trajectory

The DSMC method was applied to 13 different altitudes, separated by 5 km intervals along both the upleg and downleg trajectories. For each altitude, three different rocket orientations were simulated, the ram, crosstrack and wake orientation as described in Sec. II.A.

A. Density Fields

Figure 4 shows the DSMC number density contours at 80 km upleg and downleg, depicting side and nadir views corresponding to the three orientations described above. The effect of rocket orientation is readily apparent in these plots. Note the significant amount of disturbance surrounding the ATOX sensors at the ram orientation caused by the asymmetric shock wave. In general, the shock wave acts to compress the measurement volume on the ram side of the payload and rarefy the measurement volume on the wake side of the payload module, creating large variances in atomic and molecular species concentrations with orientation.

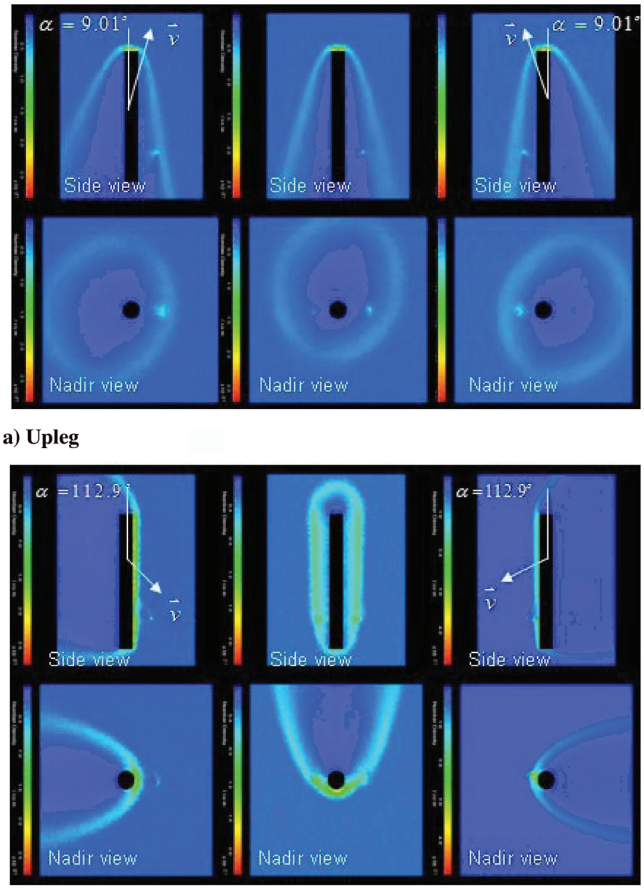

a) Upleg

b) Downleg

Fig. 4 Number density contours at 80 km; ram, wake and crosstrack orientations.

Figure 5 shows DSMC contour plots of number density with respect to upleg and downleg altitudes in the ram direction. The number density contours at 80 and 90 km contain relatively distinct bow shocks, whereas the shock layers for the remaining altitudes become increasingly diffuse. From Table 1, λ_∞ changes by 4 orders of magnitude from 80 to 140 km. With increased altitude and the accompanying increase in flow rarefaction, the thickness of the bow shock wave increases. The thickness is roughly proportional to several mean free paths [22]. As the flight progresses, the velocity vector is slowly rotated with respect to the payload module minor spin axis, creating a continually more robust ram/wake effect. This in turn creates a continual shift in measured concentrations even within each of the three attitude measurements. These aerodynamic disturbances clearly impact the ability of the ATOX sensor system to collect accurate freestream atomic oxygen concentrations.

B. Atomic Oxygen Concentration in the Sensor Volume

To better quantify the aerodynamic influences on the atomic oxygen measurements, the disturbed atomic oxygen concentrations were computed and averaged over the appropriate solid angles corresponding to regions A and B in Fig. 1b. Figure 6 shows the numerically computed DSMC atomic oxygen concentrations as functions of altitude and orientation for both the upleg and downleg trajectories. The results of the simulations plotted in Fig. 6 clearly

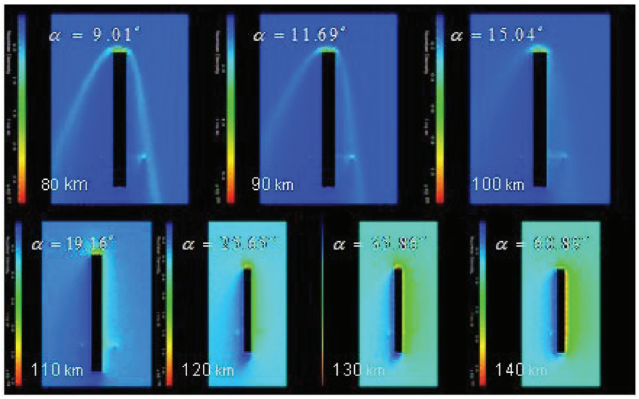

a) Upleg

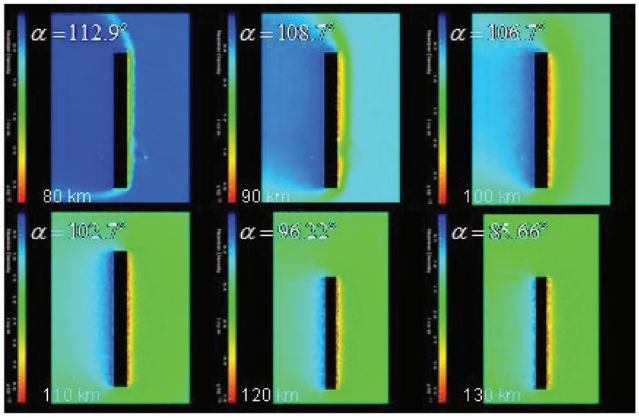

b) Downleg

Fig. 5 Number density contours in the ram direction as a function of altitude.

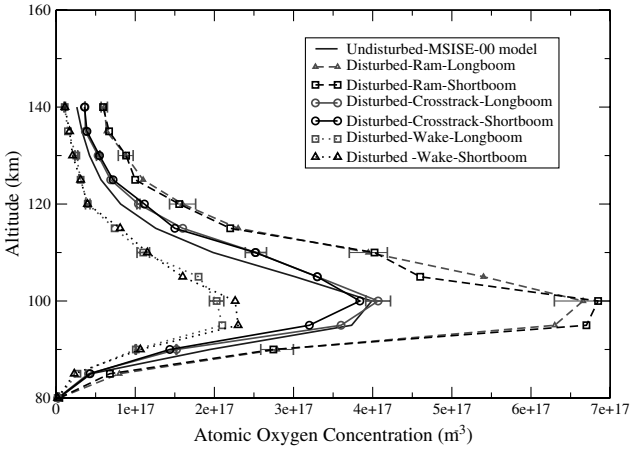

a) Upleg trajectory

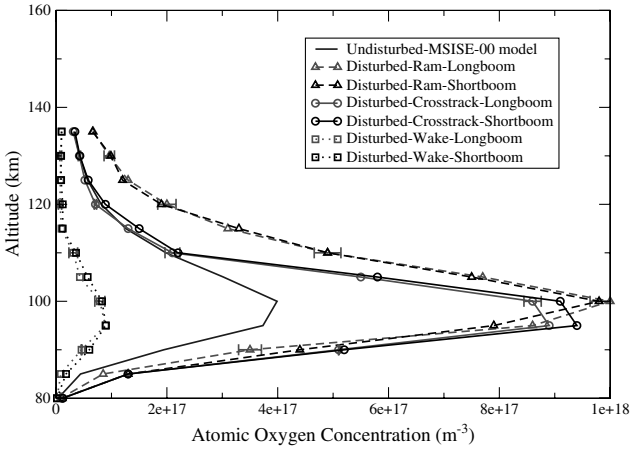

b) Downleg trajectory

Fig. 6 Disturbed vs undisturbed atomic oxygen concentrations as function of altitude and orientation.

show that the data collected in each of the ram, crosstrack, and wake directions vary significantly from actual free steam conditions. In general, concentration measurements made in the ram and crosstrack directions appear larger than actual freestream concentrations, whereas measurements made in the wake direction appear lower than actual freestream concentrations. Although not clearly visible from the plots, due to large scale differences, the largest upleg variation with respect to both volumes A and B occurred at 140 km altitude, ram direction with values of 126% and 132%, respectively. The largest downleg variation for volumes A and B also occurred at 140 km altitude, but in the crosstrack direction with differences of 229% and 202%, respectively. As expected, only minor variations are seen as a result of boom length differences.

For comparison purposes, the NS-slip results corresponding to 80 and 90 km upleg were compared with the DSMC results obtained using 2.0E6 simulated molecules and are shown in Fig. 7. These results show a line of atomic oxygen concentrations extending perpendicular from the payload surface to the end of the flow domain ($x = 2.011$ m, $y > 0.22$ m, $z = 0$). As expected, the 80 km results show better agreement than the 90 km results, although neither are at all locations within 20% of the DSMC results. The reason for the significant errors seen at 90 km altitude is likely due to the limitations of the NS-slip method as the Knudsen number approaches the noncontinuum limit.

Further inspection of the 80 km DSMC case, specifically at $y > 1$, reveals a significant amount of statistical scatter (scatter $\propto \frac{1}{\sqrt{N}}$). Therefore, the standard deviation σ

$$\sigma = \sqrt{\frac{\sum^{n}(x_i - \bar{x})}{n-1}} \tag{7}$$

of number density in the sensor control volume for the long boom are plotted in Fig. 6.

Several additional DSMC simulations were thus carried out for the 80 and 90 km altitudes. These simulations were done for the ram orientation only and used a successively larger number of simulated molecules. The results of these simulations are plotted in Fig. 8. The additional simulations at 80 km included 2.0E6, 4.0E6, and 8.0E6 simulated molecules. As shown in Fig. 8a, relative improvement was not achieved until $N = 8.0$E6. In contrast, the scatter at 90 km, shown in Fig. 8b, shows remarkable improvement with $N = 4.0$E6. Extending the 80 km simulations to even higher levels of N was not conducted, and seemed impractical because, for all values of N, the statistical scatter was centered around a true mean value.

C. Correction of the Aerodynamic Effects

As shown in Sec. IV.B, the number density of atomic oxygen measured in the control volume deviates considerably from the number density in the freestream. Therefore, following the approach of Rapp [1], the density measured by the ATOX sensor needs to by corrected by a ram-factor f_{ram}

$$n = f_{\text{ram}} \cdot n_{\text{meas}} \tag{8}$$

where n_{meas} is the density measured by the instrument and n is the undisturbed atmospheric density. Based on our three-dimensional simulations, we have determined altitude profiles of the ram-factors for both sensors, booms, and all orientations. The ram-factor is determined from the volume average of the atomic oxygen densities and its value for both ATOX sensors and the three different orientations is plotted in Fig. 9.

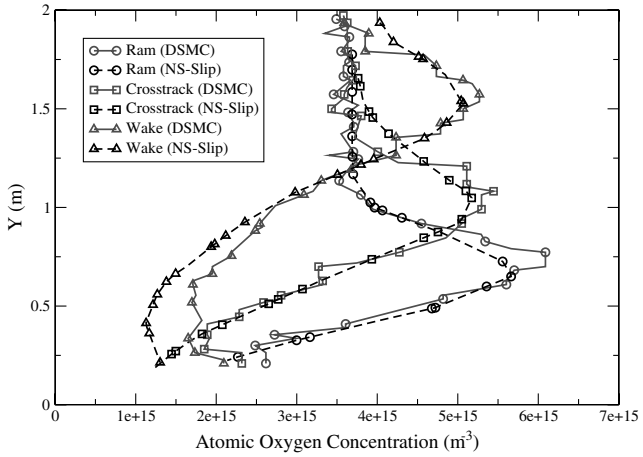

a) 80 km

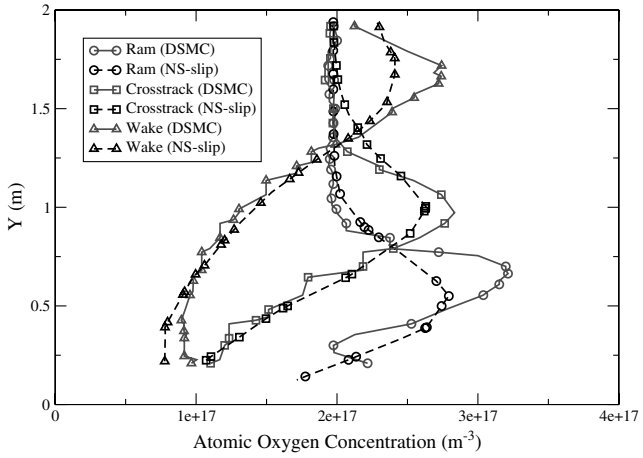

b) 90 km

Fig. 7 Comparison plots using DSMC and NS-slip methods ($x = 2.01$, $y > 0.22$, $z = 0$).

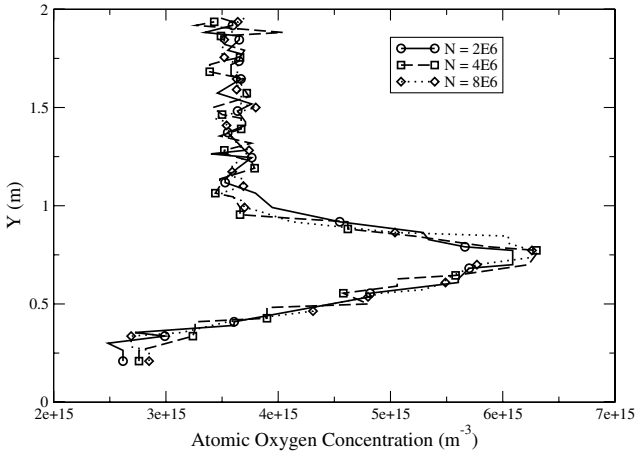

a) 80 km

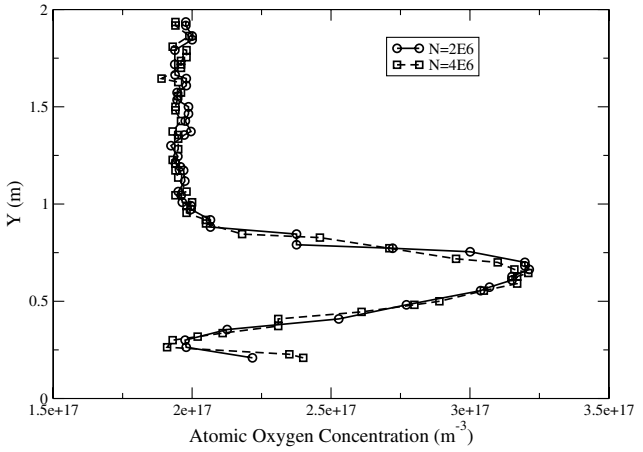

b) 90 km

Fig. 8 DSMC results in ram direction, showing effect of increased N on statistical scatter.

In Fig. 10, the correction factors plotted in Fig. 9 are applied to the upleg of the CODA II mission. The wake measurements are excluded because the sensor scientists are doubting the validity of their data for the wake orientation of the ATOX sensor. The downleg data are not shown because effects of the Doppler shift may need to be accounted for in a correction of the sensor data.

The results clearly indicate that the effects due to orientation are substantially minimized. The maximum atomic oxygen concentration occurred at approximately 93.5 km and resulted in a 17% variance between ram and crosstrack orientations. This variance was reduced to 2% by application of the correction factors obtained through the numerical simulations. At 90 km altitude, the uncorrected vs corrected results were 21% and 8%, respectively. The plots further indicate that the lower altitudes (below the concentration peak) resulted in far better agreement than the upper altitudes (above 90 km), although the corrected data sets still showed remarkable improvement over their uncorrected counterparts.

The difference to the MSISE-00 model above the peak of the atomic oxygen concentration can be explained with the purpose of the mission. Because this mission was launched to study the effects of the aurora on the neutral atmosphere, differences to the atmospheric model were expected. During a geomagnetic storm, energetic particles stream into the auroral regions. These particles collide with neutrals in the 110–140 km region, resulting in both spectacular auroral displays and the dull glow of diffuse aurora. It is thought that local heating of the atmosphere by the aurora drives profound changes in the upper atmosphere. The atomic oxygen measurements during the CODA II mission were performed to see if changes could be observed in the atomic oxygen layer. The atomic oxygen layer should be shaped by diffusive equilibrium, and changes in the vertical profile could indicate mixing driven by the aurora. This seems to be indicated by the corrected sensor data in Fig. 10.

V. Conclusions

In this paper, we have presented a numerical approach to compute absolute atomic oxygen densities from rocket-borne ATOX sensor measurements. Increased computing power helps to quantify the relationship between the disturbed and undisturbed regions immediately surrounding sounding rocket payloads. The effects of flow field disturbances were examined with respect to atomic oxygen concentrations in the lower thermosphere, and specifically applied to the CODA I and CODA II geometries. These influences were numerically simulated via DSMC and Navier–Stokes methods. Like the raw data sets, the numerical results predicted that the relative magnitudes of disturbed vs undisturbed atomic oxygen concentrations were highly dependent on rocket orientation. The Navier–Stokes equations with first-order slip wall boundary conditions simulated along the upleg, near-continuum altitudes showed fair agreement with the DSMC method at 80 km and served to illustrate the severe limitations of this method as larger Knudsen numbers are reached. The correction factors were applied to the upleg portion of the CODA II experimental data set and shown to substantially reduce the effects of boom orientation.

The steady-state results presented herein consist of numerical simulations computed at 5 km intervals. Because the rocket is spin stabilized at 1 revolution/s, this relatively large interval width allows an average of 5 revolutions per interval. There may be

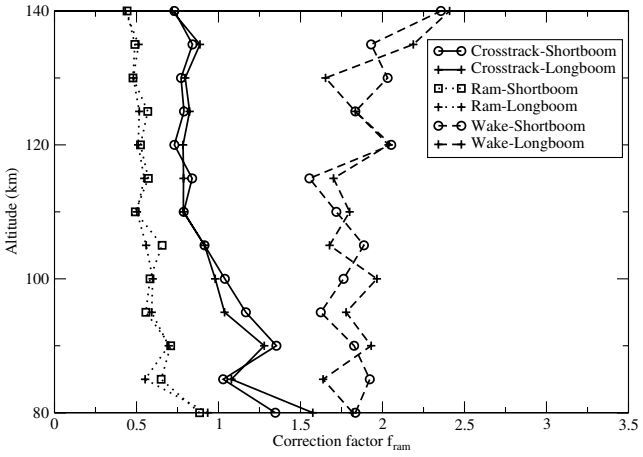

a) Ram factor for the upleg

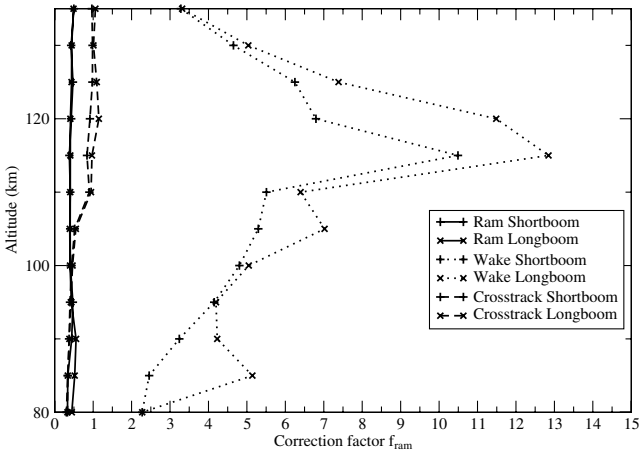

b) Ram factor for the downleg

Fig. 9 Altitude profiles for the CODA II mission.

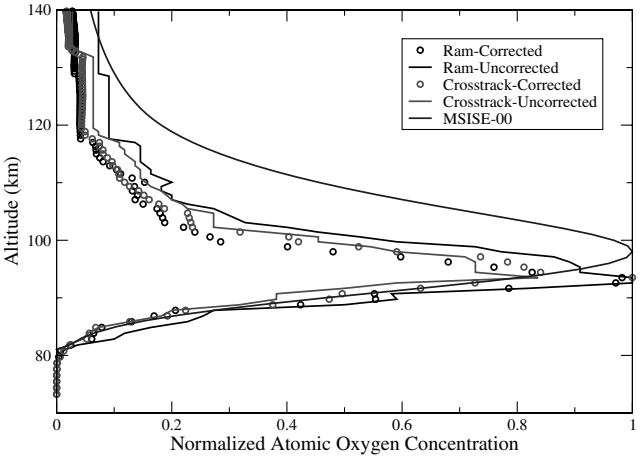

Fig. 10 Correction of ram and crosstrack direction for upleg of CODA II mission.

significant effects due to the coarseness of the intervals and unsteadiness that are presently unaccounted for. We are currently advancing this work by conducting simulations in the unsteady regime. This future research will serve to provide simulations for all points in time along the entire trajectory.

Future work will account for additional causes of atomic oxygen variations, including Doppler and contamination effects. These and the present flow field disturbance research will be applied to existing CODA I and II data sets and act as "correction functions" to derive better freestream atomic oxygen concentration statistics within the lower thermosphere.

Acknowledgment

This work was supported by the Space Dynamics Laboratory (http://www.sdl.usu.edu) under a grant from the enabling technologies program.

References

[1] Rapp, M., Gumbel, J., and Lübken, F.-J., "Absolute Density Measurements in the Middle Atmosphere," *Annales Geophysicae*, Vol. 19, No. 5, 2001, pp. 571–580.

[2] Ulwick, J. C., "A Rocket Investigation of Mesospheric Eddy Diffusion Effects on Airglow and Oxygen Chemistry," NASA, TR 20020005972, Nov. 2001.

[3] Gumbel, J., and Witt, G., "Monte Carlo Studies of the Resonance Fluorescence Technique for Atmospheric Atomic Oxygen Measurements," *Journal of Quantitative Spectroscopy and Radiative Transfer*, Vol. 58, July 1997, pp. 1–17.

[4] Patterson, P., "In Situ Measurements of Upper Atmospheric Oxygen: The ATOX Resonant Flourescence/Absorption Sensor," Ph.D. Thesis, Utah State Univ., Logan, UT, 2005.

[5] Gumbel, J., "Aerodynamic Influences on Atmospheric in situ Measurements from Sounding Rockets," *Journal of Geophysical Research*, Vol. 106, No. 6, 2001, pp. 553–564.

[6] Ridley, B., Davenport, J., Stief, L., and Welge, K., "Resonance Line Broadening in Helium Discharge Lamps," *Journal of Chemical Physics*, Vol. 57, July 1972, p. 520.

[7] Zuber, A., "Resonance Light Sources and Their use in Atmospheric Research," Ph.D. Thesis, Univ. of Stolkholm, Sweden, 1989.

[8] Patterson, P., Swenson, C., Clemmons, J., Christensen, A., and Gregory, J., "Atomic Oxygen Erosion Observations in a Diffuse Aurora," *EOS Transaction, Fall Meeting Supplement*, Abstract SA21A-02, American Geophysical Union, San Francisco, Dec. 2003.

[9] Sun, Q., Cai, C., Boyd, I., Clemmons, J., and Hecht, J., "Computational Analysis of High-Altitude Ionization Gauge Flight Measurements," *Journal of Spacecraft and Rockets*, Vol. 43, No. 1, 2006.

[10] Gridgen: Reliable CFD Meshing, Pointwise, Inc., Fort Worth, TX, http://www.pointwise.com/gridgen, Dec. 2005.

[11] Hedin, A. E., "Extension of the MSIS Thermospheric Model into the Middle and Lower Atmosphere," *Journal of Geophysical Research*, Vol. 96, No. A2, 1991, pp. 1159–1172.

[12] Maxwell, J. C., "On Stresses in Rarefied Gases Arising from Inequalities in Temperature," *Philosophical Transactions of the Royal Society of London*, Vol. 170, No. 1, 1979, pp. 231–256.

[13] Reni, R., and Subrata, R., "Numerical Study of Heat Transfer in High Speed Microflows," *36th AIAA Thermophysics Conference*, AIAA, Reston, VA, June 2003.

[14] Bird, G. A., *Molecular Gas Dynamics and the Direct Simulation of Gas Flows*, Oxford Univ. Press, New York, 1994.

[15] Ivanov, M. S., and Gimelshein, S. F., "Computational Hypersonic Rarefied Flows," *Annual Review of Fluid Mechanics*, Vol. 30, Jan. 1998, pp. 469–505.

[16] Rault, D. F. G., "Aerodynamics of the Shuttle Orbiter at High Altitudes," *Journal of Spacecraft and Rockets*, Vol. 31, No. 6, 1994, pp. 944–952.

[17] Hass, B. L., and Schmitt, D. A., "Simulated Rarefied Aerodynamics of the Magellan Spacecraft During Aerobraking," *Journal of Spacecraft and Rockets*, Vol. 31, No. 6, 1994, pp. 980–985.

[18] Moss, J. N., Blanchard, R. C., Wilmoth, R. G., and Braun, R., "Mars Pathfinder Rarefied Aerodynamics: Computations and Measurements," *Journal of Spacecraft and Rockets*, Vol. 36, No. 3, 1999, pp. 330–339.

[19] Oran, E. S., Oh, C. K., and Cybyk, B. Z., "Direct Simulation Monte Carlo: Recent Advances and Applications," *Annual Review of Fluid Mechanics*, Vol. 30, Jan. 1998, pp. 403–441.

[20] Bird, G. A., *DS3G Program User's Guide*, Ver. 1.1, Killara, New South Wales, U.K., 2003.

[21] Tannehill, J. C., and Eisler, R. R., "Numerical Computation of the Hypersonic Leading Edge Problem Using the Burnett Equations," *Physics of Fluids (1958-1988)*, Vol. 19, No. 1, 1976, pp. 10–15.

[22] Sun, Q., Cai, C., Boyd, I., Clemmons, J., and Hecht, J., "Computational Analysis of High-Altitude Ionization Gauge Flight Measurements, AIAA Paper 2004-2686, July 2004.

A. Ketsdever
Associate Editor